First-principles study on the interaction of H interstitials with grain boundaries in α- and γ-Fe

Yaojun A. Du,[1] Lars Ismer,[2] Jutta Rogal,[1,*] Tilmann Hickel,[2] Jörg Neugebauer,[2] and Ralf Drautz[1]

[1]*Interdisciplinary Centre for Advanced Materials Simulation, Ruhr-Universität Bochum, D-44780 Bochum, Germany*
[2]*Max-Planck-Institut für Eisenforschung, Max-Planck-Straße 1, D-40237 Düsseldorf, Germany*

The presence of hydrogen may weaken the bonding of iron atoms at grain boundaries, leading to intergranular embrittlement and thus failure of the bulk material. In this paper, we study the interaction of hydrogen interstitials with close-packed and open grain boundary structures in α- and γ-Fe using density-functional theory. We find that hydrogen accommodation within the grain boundaries strongly depends on the local coordination of the available interstitial sites. Within the open grain boundary structures larger interstitial sites are available, enhancing the solubility as compared to that in the respective bulk phases. The mobility of hydrogen within the investigated grain boundaries is low compared to diffusion in perfect single-crystalline bulk. The grain boundaries do not provide fast diffusion channels for hydrogen, but act as hydrogen traps. Hydrogen that is accumulated within the grain boundaries can lead to a lowering of the critical strain required to fracture the material.

PACS number(s): 81.40.Np, 75.50.Bb, 61.72.Mm, 71.15.Mb

I. INTRODUCTION

Iron-based metallic alloys and steels have a long tradition as highly important structural materials. Their characteristics are continuously improved in order to fulfill increasingly specific and stringent requirements. For most applications, the mechanical properties of steel are of particular interest. They are influenced decisively by the composition and microstructure of the material. In particular, modern high-strength steels are characterized by a combination of different phases (ferrite, austenite, or martensite) as well as a large number of grain and phase boundaries that govern hardening mechanisms such as TRIP (transformation induced plasticity), TWIP (twinning induced plasticity), SBIP (shear banding induced plasticity), or MBIP (microbanding induced plasticity).

Defects and impurities play an important role as they may contribute to improving or degrading the performance of a steel. Previous experimental and theoretical studies showed that impurities within iron grain boundaries (GBs) significantly affect the intergranular cohesion.[1–7] For example, interstitial carbon and boron impurities enhance cohesion,[1,4] while sulfur and phosphorous interstitials are embrittlers.[5] Regarding substitutional transition metal impurities, molybdenum was shown to enhance intergranular cohesion, while palladium acts as an embrittler.[2]

Hydrogen atoms, which can be absorbed into steel during production and service, have a detrimental embrittling effect on the mechanical properties of iron and steels. This so-called hydrogen embrittlement (HE)[8] is a complex problem and to date has not yet been fully understood. In particular, it is still unclear to what extent HE is affected by the microstructure of a material. Previous observations that hydrogen atoms are trapped by vacancies, dislocations, and grain boundaries[9–12] led to considerations on superabundant vacancy formation,[13] hydrogen-enhanced local plasticity,[14–17] and hydrogen-enhanced decohesion (HEDE).[18–22]

In the HEDE mechanism, hydrogen atoms segregate to microstructural features such as grain boundaries, and form a locally increased concentration of hydrogen. At the grain boundary, the interaction between Fe atoms tends to be weaker than in the bulk material and a high concentration of hydrogen

atoms may further weaken the bonding across the interface, which may lead to a significantly reduced cohesive strength of the material. Currently, knowledge about the relevance of HEDE is still insufficient. This is mainly due to the fact that the experimental observation of hydrogen impurities is difficult due to their low solubility and high mobility in iron and steel.

Theoretical studies of hydrogen interaction with Fe grain boundaries have so far been limited to the ferritic α-phase. Gesari *et al*.[23] computed the binding energy between H and the $\Sigma 5[001](310)$ grain boundary in the α-phase using a semiempirical atom superposition and electron delocalization molecular orbital (ASED-MO) formalism.[24] They showed that the Fe grain boundary traps H interstitials. Zhong *et al*.[12] studied the interaction between H and the $\Sigma 3[1\bar{1}0](111)$ α-Fe grain boundary and the corresponding surface using density-functional theory (DFT)[25,26] calculations. They compared the binding energy of H to the grain boundary and to the associated free surface to characterize the decohesion effect of impurities on the grain boundary structure.[27,28] Their results suggest that H is a strong embrittler for the $\Sigma 3$ grain boundary structure in α-Fe.

Within this paper, we perform a more detailed DFT study of the influence of the microstructure on HE and in particular of the HEDE mechanism. We focus on two important phases for steels—the ferritic α- [body-centered cubic (bcc)] and the austenitic γ-phase [face-centered cubic (fcc)]. Both phases are relevant for traditional as well as modern high-strength steels. In TWIP and TRIP steels,[29–31] for example, the fcc structure is stabilized by alloying elements such as Mn. In these and many other steels, the bcc structure also occurs in the tetragonally distorted form of the α'-phase in the martensitic phase. While the mechanical properties of α-Fe do suffer from HE, γ-Fe with a fcc crystal structure is sometimes considered to show a better resistance against degradation by HE.[32] However, it has been shown recently that some austenitic steels—depending on the chemical composition—also exhibit significant hydrogen enhanced crack growth.[33,34] While α-Fe is ferromagnetic, the magnetic structure of γ-Fe is in experiments[35] and first-principles calculations[36,37] found to exhibit a spin-spiral magnetic ground state with a tetragonally

TABLE I. Interface energies γ_{GB}, lattice parameters (in Å) of the relaxed supercells, as well as tilt axes, grain boundary planes, and misorientation angles Θ for all four grain boundaries. In the first column, the number of atoms in the corresponding supercell is also given.

	γ_{GB} (J/m^2)	a	b	c	α,β	γ	Tilt axis	GB plane	Θ
$\Sigma 3$ bcc (24 atoms)	0.47	4.00	2.44	27.98	90°	90°	[1$\bar{1}$0]	(112)	70.0°
$\Sigma 3$ fcc (36 atoms)	−0.21	4.21	2.43	35.74	90°	90°	[1$\bar{1}$0]	(111)	70.5°
$\Sigma 5$ bcc (40 atoms)	1.53	4.67	4.67	36.57	90°	35°	[001]	(310)	36.8°
$\Sigma 11$ fcc (88 atoms)	0.5	8.10	2.44	45.83	90°	90°	[1$\bar{1}$0]	(113)	129.5°

distorted fcc lattice; see, for example, Ref. 38. At temperatures relevant for applications the γ-phase of steels is, however, paramagnetic and to a first approximation may be treated as nonmagnetic in the simulations.[39]

Due to the computational cost of the DFT calculations, we have to limit ourselves to a few grain boundaries in the α- and γ-phase. One important aspect that we address in this paper is the correlation between available interstitial sites and hydrogen solution enthalpies. It has been pointed out previously that local volumetric effects can dominate the solution energies of H interstitials.[39] The aim is therefore to investigate if a similar trend also holds for the solution energies near grain boundaries in bcc as well as fcc iron. To directly compare the influence of the local geometric structure, we chose the $\Sigma 3[1\bar{1}0](112)$ bcc and $\Sigma 3[1\bar{1}0](111)$ fcc Fe grain boundaries as representatives for dense and the $\Sigma 5[001](310)$ bcc and $\Sigma 11[1\bar{1}0](113)$ fcc Fe grain boundaries as examples for more open interface structures. These grain boundaries are also relevant, since they have a low formation energy in the respective phases as previously shown in the case of bcc-Fe[40] and in several fcc systems such as Al.[41]

A second important aspect is the diffusion of H interstitials within various grain boundaries. Our results obtained for these very different structures allow us to investigate the dominating factors that determine the solubility and mobility of H interstitials near grain boundaries and to gain insight into the underlying mechanisms of HE.

The paper is organized as follows. The computational approach and supercell models for the various Fe grain boundaries are detailed in Sec. II. The formation energies, local geometries, and local magnetic moments of the clean grain boundary structures are discussed in Sec. III. In Sec. IV, the interaction of H impurities with the grain boundaries is detailed and a discussion of the decohesion effect of H on the grain boundaries is presented in Sec. V. H migration in the vicinity of the grain boundaries is illustrated in Sec. VI. We conclude the paper with a discussion and summary of our results in Sec. VII.

II. COMPUTATIONAL DETAILS AND STRUCTURAL MODELS

Density-functional theory calculations were performed employing the projector augmented-wave (PAW) method[42,43] as implemented in the VASP code.[44,45] For the exchange-correlation functional, the generalized gradient approximation (GGA, PW91)[46,47] was used. Two PAW potentials were tested: one treating the $3p$ electrons explicitly as valence electrons with an energy cutoff for the plane waves, E_{cut}, of 350 eV, and a second one including the $3p$ electrons

in the pseudopotential requiring a lower cutoff energy of 270 eV. Both approaches gave consistent results. The Brillouin zone integration was performed using the Monkhorst-Pack[48] scheme with a partition length of 0.11 bohr^{-1} or smaller in each direction, resulting in k-point meshes of [6 × 10 × 1] for bcc $\Sigma 3$, [5 × 10 × 1] for fcc $\Sigma 3$, [10 × 10 × 1] for bcc $\Sigma 5$, and [3 × 10 × 1] for fcc $\Sigma 11$ as listed in Table I. The computational setup ensures that differences in the solution energies of H interstitials and formation energies of Fe grain boundaries are converged to within 10 meV and 0.1 J/m^2, respectively. The calculations for ferromagnetic α-Fe were performed including spin polarization. For the γ-phase, the experimental situation of zero net magnetic moment is approximated by nonmagnetic calculations. Although numerical schemes to treat paramagnetic structures in DFT calculations are available,[49,50] their application to the defect structures considered here is currently not feasible. Furthermore, we observed, e.g., for Fe-Mn systems that the change in the H energetics caused by different magnetic configurations is partially compensated by induced changes in the lattice constants, allowing us to neglect the magnetic effects and estimate the properties using nonmagnetic calculations.[39]

For the ferromagnetic α-iron we obtain an equilibrium lattice constant of 2.85 Å, which is in good agreement with the experimental value of 2.867 Å[51] and previous theoretical results of 2.83–2.87 Å.[52–55] As an example for a dense, low energy interface structure in bcc iron, the $\Sigma 3[1\bar{1}0](112)$ grain boundary (in the following termed $\Sigma 3$) is chosen, which is constructed by rotating the crystal along the [1$\bar{1}$0] tilt axis with a misorientation angle of 70° where the grain boundary interface is in the (112) plane; cf. Table I. The more open $\Sigma 5[001](310)$ grain boundary ($\Sigma 5$ in short) is constructed correspondingly using the values given in Table I.

The equilibrium lattice constant for the nonmagnetic γ-iron is 3.45 Å.[39] The $\Sigma 3[1\bar{1}0](111)$ ($\Sigma 3$ in short) represents a dense and low energy interface structure in fcc iron, corresponding to a change of the stacking sequence of the (111) layers. In contrast to that, the $\Sigma 11[1\bar{1}0](113)$ ($\Sigma 11$ in short) exemplifies a more open interface structure. Both grain boundary structures are set up using the values given in Table I. For all grain boundary structures, we fully relax the volume of the corresponding supercells and the internal coordinates. Zero-point vibration energies and the wave-like character of hydrogen are not considered in the present study.[56]

III. CLEAN GRAIN BOUNDARIES IN α- AND γ-IRON

In this section, we briefly discuss the structure and energetics of the clean grain boundaries without hydrogen impurities.

The interface energy of a grain boundary is calculated as

$$\gamma_{GB} = \frac{E_{GB}^{tot} - E_{bulk}^{tot}}{2A}.$$ (1)

Here, E_{GB}^{tot} is the energy of the n atom supercell of the grain boundary structure, E_{bulk}^{tot} is the energy of the commensurate Fe bulk supercell, and A is the area of the grain boundary interface. Due to the periodic boundary conditions, each supercell contains two equivalent grain boundary interfaces separated by sufficiently many bulk layers to avoid contributions to Eq. (1) from interactions between the grain boundaries.

A. Σ3 grain boundaries

The selected Σ3 grain boundaries represent low energy symmetric twin boundaries in bcc and fcc iron. The corresponding interface energies and setup of the supercells are listed in Table I. The structures are shown in Figs. 1(a) and 1(b).

The interface energy of the Σ3 grain boundary in bcc iron has a value of 0.47 J/m² and compares reasonably well to previous DFT results of 0.34 J/m² in Ref. 40. In fcc iron, the interface energy of the Σ3 grain boundary is negative: −0.21 J/m². This is consistent with the negative intrinsic stacking fault energy of pure iron[57] and the fact that γ-Fe is only stable in the temperature range between 1184 and 1673 K, but not at 0 K. The consideration of this grain boundary is still meaningful, since in modern austenitic steels, where the bulk fcc phase is stabilized by alloying elements, a high volume fraction of twinned material is often observed.[58] The impurity induced changes in the formation energy are typically also well described in the regime of negative formation energies.[59]

The fact that the Σ3 twin boundaries exhibit low interface energies can readily be understood when analyzing structural properties of these nearly close-packed interfaces: both Σ3 twin boundaries introduce only relatively small deviations in the local coordination and interatomic distances as compared to the corresponding bulk lattices. The deviations of the Voronoi volumes of interstitial sites at the interface (5.98 Å³ in Σ3 bcc and 5.25 Å³ in Σ3 fcc) as compared to the preferred interstitial sites in the bulk phases (5.81 Å³ for tetrahedral sites in bcc and 5.12 Å³ for octahedral site in fcc) are with 3% an order of magnitude smaller than the deviations for the more open grain boundaries discussed below. In ferromagnetic bcc Fe, the small distortion of the lattice is also reflected in the variation of the local magnetic moment close to the interface region; cf. Fig. 2(a). Directly at the interface, the magnetic moment is slightly enhanced by 0.15 μ_B, but already in the third layer from the interface it is equal to the bulk value of 2.2 μ_B. The figure also illustrates that the magnetic properties are correlated to the interlayer distances close to the twin boundary and therefore the excess volume of the respective atoms.

B. Σ5 and Σ11 grain boundaries

The Σ5 grain boundary in bcc Fe and the Σ11 grain boundary in fcc Fe represent symmetric tilt grain boundaries with more open interface structures compared to the Σ3 grain boundaries [see also Figs. 1(c) and 1(d)], yielding considerably different local coordinations and nearest-neighbor distances.
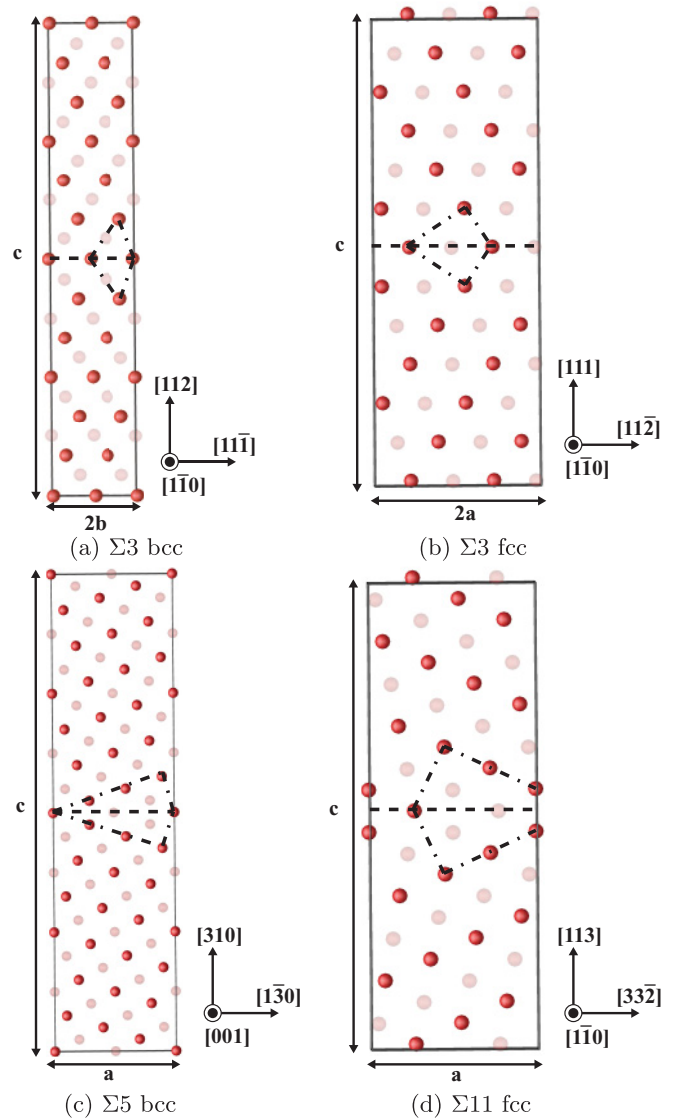

FIG. 1. (Color online) Supercells for the grain boundaries considered in the present study. The structures of the Σ3 grain boundaries in bcc and fcc iron are shown in (a) and (b), respectively. The more open interface structures of the Σ5 in bcc and Σ11 in fcc iron are shown in (c) and (d). Atoms shaded in a lighter color are on a different plane along the b axis. The dashed-dotted lines indicate available voids at the respective interfaces.

In both grain boundaries within the boundary plane, relatively large cavities are formed that deviate in both cases by ~20% in Voronoi volume (6.85 Å³ in Σ5 bcc and 6.31 Å³ in Σ11 fcc) from the interstitial sites in the bulk phases (5.81 Å³ for tetrahedral sites in bcc and 5.12 Å³ for octahedral sites in fcc). These cavities provide low energy interstitial sites for hydrogen as we discuss in Sec. IV.

The distortion of the atomic structure close to the grain boundary is also reflected in the variation of the local magnetic moments in ferromagnetic bcc Fe. Here, the effect is much larger than for the Σ3 grain boundary. As also discussed by Cák *et al.*,[53] the increase of the magnetic moment by 0.3 μ_B for Fe atoms at the grain boundary can mainly be explained by a magnetovolume effect, i.e., a larger atomic volume causes
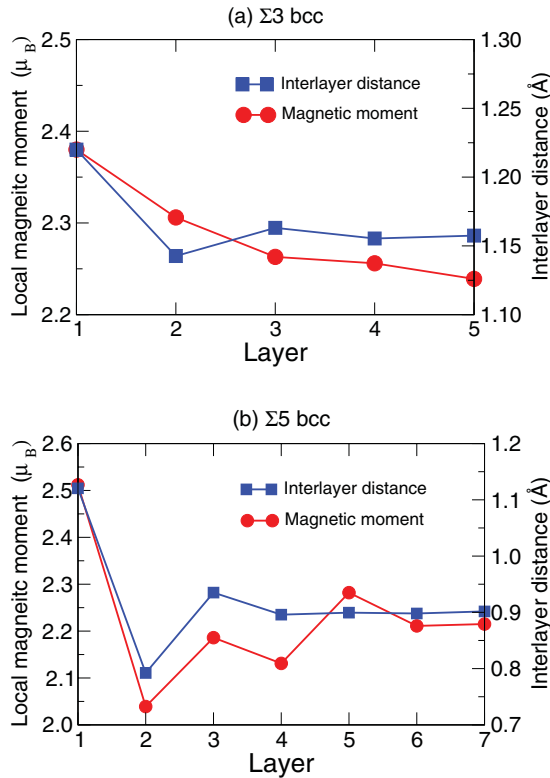
FIG. 2. (Color online) Comparison of the local magnetic moments and the interlayer distance of Fe atoms at various layers from a clean (a) $\Sigma 3$ and (b) $\Sigma 5$ grain boundary in α-iron.

TABLE II. Solution energy ΔE of H in various intermediate (im) and interface (if) interstitial sites in the fcc $\Sigma 3$ (36 atom supercell) and bcc $\Sigma 3$ (144 atom supercell) Fe grain boundaries. Geometrical data provided include the distance z from the interface, the distances l of H from the nearest-neighbor Fe atoms, and the corresponding Voronoi volume V.

Site	z (Å)	l (Å)	V (Å³)	ΔE (eV)
fcc-im1	1.04	1.77 1.77 1.77 1.77 1.78 1.78	5.58	0.18
fcc-im2	3.03	1.78 1.78 1.78 1.80 1.80 1.80	5.75	0.10
fcc-im3	5.01	1.77 1.77 1.78 1.78 1.78 1.79	5.65	0.11
fcc-im4	7.01	1.78 1.78 1.78 1.78 1.78 1.79	5.67	0.09
fcc-im5	8.99	1.78 1.78 1.78 1.78 1.78 1.79	5.66	0.10
fcc-bulk		$(1.78)_6$	5.63	0.05
bcc-if1	0.00	1.74 1.74 1.81 1.81 2.03 2.03	6.46	−0.18
bcc-im1	1.20	1.66 1.66 1.67 1.67	6.74	0.10
bcc-im2	1.39	1.65 1.65 1.72 1.73	6.52	0.05
bcc-im3	2.06	1.65 1.67 1.67 1.67	6.51	0.09
bcc-im4	3.52	1.65 1.65 1.66 1.66	6.41	0.21
bcc-im5	4.69	1.65 1.65 1.66 1.66	6.40	0.24
bcc-im6	5.56	1.64 1.65 1.65 1.68	6.40	0.21
bcc-im7	6.99	1.65 1.65 1.66 1.66	6.39	0.23
bcc-bulk		$(1.66)_4$	6.46	0.25

an increase in the magnetic moment. However, the atomic volume is not the only factor, since the magnetic moment as a function of layers from the grain boundary interface shows an oscillatory behavior, whereas the local volume of the Fe atoms decreases smoothly. The oscillations in the magnetic moment are more closely related to the local coordination as reflected in the interlayer distance, which also oscillates;[60] cf. Fig. 2.

The large structural and magnetic deviations from the bulk properties lead to significantly higher interface energies, as provided in Table I. The $\Sigma 5$ grain boundary in bcc Fe has an interface energy of 1.53 J/m^2, which is consistent with previous DFT results of 1.49 J/m^2 (Ref. [40]) and 1.63 J/m^2 (Ref. [53]). Also, the interface energy of the $\Sigma 11$ grain boundary in fcc Fe is much higher than the corresponding value for the $\Sigma 3$ grain boundary. However, the absolute value of 0.50 J/m^2 is still rather small. This is consistent with results for other nonmagnetic fcc metals, where $\Sigma 11$ was also identified as the grain boundary with the lowest formation energy,[41] apart from $\Sigma 3$.

IV. HYDROGEN SOLUTION ENERGIES IN α- AND γ-IRON GRAIN BOUNDARIES

The solubility of H within Fe bulk can be characterized by the solution energy, ΔE, defined as

$$\Delta E = E_{\text{Fe}_n\text{H}}^{\text{tot}} - E_{\text{Fe}_n}^{\text{tot}} - 1/2 E_{\text{H}_2}^{\text{tot}}, \qquad (2)$$

where $E_{\text{Fe}_n}^{\text{tot}}$ is the energy of the impurity free supercell with n Fe atoms, $E_{\text{Fe}_n\text{H}}^{\text{tot}}$ is the total energy of the same supercell

with one H interstitial, and $E_{\text{H}_2}^{\text{tot}}$ is the energy of a H$_2$ molecule in vacuum. In the following, we discuss different aspects that influence the solubility of hydrogen within grain boundary regions, focusing specifically on the local coordination and the volume of the available interstitial sites.

We first compute the H solution energy within α- and γ-Fe bulk using the equilibrium lattice constant of the pure phases, respectively. In α-Fe, the most favorable interstitial site for H is the tetrahedral site (T site). For this site, we obtain a H solution energy (ΔE) of 0.25 eV for a 128 atom supercell, which is in good agreement with Jiang *et al.*[54] who computed a solution energy of 0.20 eV. In γ-Fe, hydrogen prefers the octahedral site (O site). The nonmagnetic calculations employed here yield a solution energy of 0.05 eV for a 32 atom supercell consistent with previous results[39] using up to 108 atom supercells.

We further studied how the bulk solution energy depends on the lattice constant. The solution energy shows a strong dependence on the Voronoi volume that is available for the incorporation of H at the respective site,[39] cf. solid lines in the graphs in Fig. 6, with a very similar trend for the tetrahedral site in bcc Fe and the octahedral site in fcc Fe.

A. Hydrogen interactions with $\Sigma 3$ grain boundaries

As discussed in the previous section, the $\Sigma 3$ grain boundaries are nearly close-packed with interstitial sites that are only up to 3% larger in volume than in the respective bulk structures. We placed H into all relevant interstitial sites of the $\Sigma 3$ grain boundary supercells. Both structures, bcc and fcc, exhibit several inequivalent local minima for the solution energy at various distances from the interface; details are given in Table II.

Looking at the distances of the incorporated H atom to the nearest-neighbor Fe atoms, one clearly observes that for almost all interstitial sites the coordination remains the same
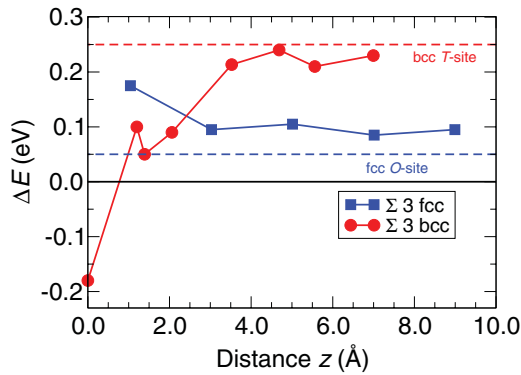
FIG. 3. (Color online) Hydrogen solution energies as a function of the distance from the grain boundary interface for the $\Sigma 3$ grain boundaries in bcc (red dots) and fcc (blue squares) Fe. The dashed lines indicate the bulk solution energies in tetrahedral sites in bcc Fe and in octahedral sites in fcc Fe, respectively.

as the respective bulk coordination, i.e., an octa/tetrahedral coordination for fcc/bcc. An exception is the site directly in the interface plane of the bcc $\Sigma 3$ grain boundary, since its coordination corresponds to a slightly elongated octahedron (cf. Fig. 7), with a relatively large nearest-neighbor distance as compared to the tetrahedral sites in bcc Fe. Such an exception is not observed for fcc Fe. The reason is that the $\Sigma 3[1\bar{1}0](111)$ fcc grain boundary corresponds simply to a change of the stacking sequence of (111) layers such that locally the character is that of an hcp lattice.

These geometrical aspects are also reflected by the solution energies, which are visualized in Fig. 3. For fcc Fe, the changes in the solution energy compared to the bulk value are moderate, since for all sites the coordination and also the Voronoi volume are almost bulk-like. The distortion of tetrahedral sites in bcc Fe is much more significant, yielding larger deviations from the bulk value. This applies in particular to the site in the interface plane, which shows a significantly lower solution energy of $\Delta E = -0.18$ eV. As a consequence, an opposite behavior of the segregation energies for the $\Sigma 3$ grain boundaries in fcc and bcc Fe is observed. While the $\Sigma 3$ grain boundary is strongly attractive for H in bcc Fe, in fcc Fe the $\Sigma 3$ boundary appears to be slightly repulsive. This might be due to the hcp character of the fcc grain boundary. The solution enthalpy of H in octahedral sites of nonmagnetic hcp Fe is 0.18 eV, which is higher than in nonmagnetic fcc bulk Fe, consistent with the behavior of the H solution energy next to the $\Sigma 3$ fcc grain boundary.

B. Hydrogen interactions with $\Sigma 5$ and $\Sigma 11$ grain boundaries

The $\Sigma 5$ grain boundary in bcc Fe and the $\Sigma 11$ grain boundary in fcc Fe are much more open structures compared to the $\Sigma 3$ grain boundaries and therefore exhibit also a larger variation in the available interstitial sites. Therefore, different strategies have been applied to identify the relevant interstitial sites for which the effect of H incorporation has been studied. For the fcc $\Sigma 11$ grain boundary, the complete potential energy surface for the incorporation of H into the supercell is considered; see Sec. IV C. For the bcc $\Sigma 5$ grain boundary, we initially placed H atoms at 50 different interstitial

sites within a small, 20 atom supercell to obtain a first idea of how the solution energy of hydrogen changes as a function of the distance from the grain boundary interface. The solution energies for H in inequivalent interstitial sites at various distances from the grain boundary interface were subsequently refined by calculations within a 180 atom orthorhombic $(1 \times 3 \times 1)$ supercell.[61]

The obtained data for the H interstitials at/close to the $\Sigma 5$ and $\Sigma 11$ grain boundary are summarized in Table III and visualized in Fig. 4. When approaching these two boundaries, the fcc O sites and bcc T sites become more and more distorted and different in coordination. This is associated with a drastic increase of the Voronoi volumes of some interstitial sites indicated earlier, providing even larger voids for H incorporation. As a consequence, the H solution energy in some interstitial sites is significantly lower than in the corresponding bulk phases.

In general, the solution energy decreases with decreasing distance from both open grain boundaries, showing that hydrogen segregation towards the grain boundary is energetically favored. Similar to the discussion of $\Sigma 3$ grain boundaries, the reduction in solution energy is more pronounced in bcc than in fcc Fe. With respect to the T site in bcc Fe, approximately 0.4 eV are gained by H atoms at the grain boundary. This compares well to the results of Gesari *et al.*,[23] who computed an energy gain of 0.3 eV for H in the $\Sigma 5$ grain boundary employing a semiempirical ASED-MO formalism. The negative solution energies suggest that it is energetically favorable for H to enter the crystal in order to segregate to the $\Sigma 5$ and $\Sigma 11$ interfaces.

C. Comparison of H interstitials at close-packed and open grain boundary structures

It was assumed earlier that the differences in solution energies in the various grain boundary structures can mainly be explained by geometric considerations. This assumption was based on a previous study that showed that volumetric effects are important to explain differences in local solubility for H in Fe-based alloys.[39] Since $\Sigma 5$ and $\Sigma 11$ are more open crystal structures compared to $\Sigma 3$, a lower hydrogen solution energy in these grain boundaries as compared to the $\Sigma 3$ grain boundaries is expected. However, already when comparing Figs. 3 and 4 it can be seen that the absolute values for the solution energy of H close to the bcc $\Sigma 5$ and the fcc $\Sigma 11$ grain boundary are not necessarily much lower than the corresponding values for the $\Sigma 3$ grain boundaries. In order to investigate this issue more systematically, a comparison between the two classes of grain boundaries has been performed with a focus on the complete H potential energy surface (PES) and the Voronoi volumes, which is discussed in the following.

As an example for the PES of hydrogen in the vicinity of the two different classes of grain boundaries, cuts through the PES of H within the $\Sigma 3$ and $\Sigma 11$ grain boundaries in fcc Fe are shown in Fig. 5. The PES is determined by sampling 2960 (in the case of fcc $\Sigma 3$) and 1720 (in the case of fcc $\Sigma 11$) points within the three-dimensional (3D) supercell. The sample points were chosen such that they include the local minima and saddle points of the potential energy surface and

TABLE III. Solution energy ΔE of H in various intermediate (im) and interface (if) interstitial sites in the fcc $\Sigma 11$ (88 atom supercell) and bcc $\Sigma 5$ (180 atom supercell) Fe grain boundaries, respectively. Geometrical data provided include the distance z from the interface, the distances l of H from the nearest-neighbor Fe atoms, and the corresponding Voronoi volume V.

Site	z (Å)	l (Å)	V (Å^3)	ΔE (eV)
fcc-if1	0.00	1.84 1.85 1.92 1.93 1.93 1.94	6.49	−0.01
fcc-im1	0.13	1.83 1.84 1.87 1.88 2.00 2.01	6.49	−0.05
fcc-im2	1.58	1.78 1.78 1.78 1.78 1.80 1.84	5.76	0.11
fcc-im3	2.71	1.76 1.79 1.79 1.79 1.80 1.81	5.74	0.10
fcc-im4	3.70	1.78 1.78 1.79 1.79 1.81 1.83	5.80	0.06
fcc-im5	5.78	1.78 1.78 1.78 1.78 1.80 1.80	5.71	0.07
fcc-im6	6.82	1.78 1.78 1.79 1.79 1.79 1.81	5.74	0.05
fcc-im7	7.84	1.78 1.78 1.79 1.79 1.80 1.81	5.75	0.04
fcc-im8	8.88	1.78 1.78 1.79 1.79 1.80 1.81	5.72	0.04
fcc-bulk		$(1.78)_6$	5.63	0.05
bcc-if1	0.00	1.83 1.83 1.83 1.84 1.84 2.63 2.64	7.48	−0.13
bcc-if2	0.01	1.70 1.70 1.73 1.74	7.15	0.08
bcc-if3	0.08	1.81 1.81 1.87 2.01 2.33 2.33	7.64	−0.18
bcc-im1	0.67	1.69 1.69 1.70 1.75	7.30	0.03
bcc-im2	0.70	1.66 1.70 1.86 1.86 2.15	8.12	−0.01
bcc-im3	1.14	1.69 1.69 1.75 1.76	7.36	0.11
bcc-im4[62]	2.58	1.63 1.65 1.70 1.70	6.40	0.31
bcc-im5	3.31	1.67 1.68 1.78 1.78	6.51	0.22
bcc-im6	4.52	1.64 1.64 1.67 1.67	6.45	0.29
bcc-im7	6.14	1.65 1.65 1.71 1.71	6.41	0.27
bcc-im8	7.23	1.64 1.64 1.67 1.67	6.44	0.29
bcc-im9	8.85	1.64 1.65 1.70 1.70	6.41	0.26
bcc-bulk		$(1.66)_4$	6.46	0.25

additional points nearby. For each of the sample points, a separate DFT calculation was performed, allowing for local relaxation of the surrounding Fe atoms, but fixing the position of the H atom and of far distant Fe atoms. The interpolation between the sample points used in Fig. 5 was performed with a symmetrized plane wave basis set, a tool which has been developed[63] in the framework of the S/PHI/nX *ab initio* package.[64]

The resulting PES gives a more complete picture of the geometric and energetic situation close to the grain
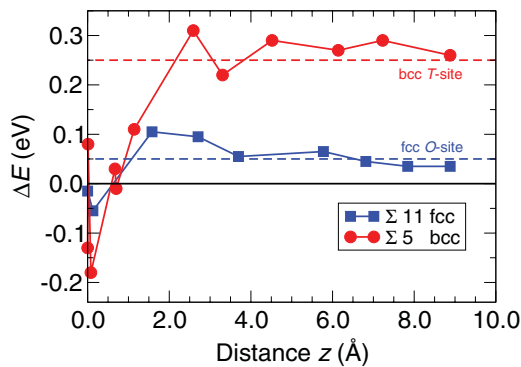

FIG. 4. (Color online) Hydrogen solution energies as a function of the distance from the grain boundary interface for the $\Sigma 5$ bcc (red dots) and $\Sigma 11$ fcc (blue squares) grain boundaries in Fe. The dashed lines indicate the solution energy in tetrahedral sites in bcc Fe and in octahedral sites in fcc Fe, respectively.

boundaries considered here as compared to the minimum energies discussed above. The local minima for H interstitials far away from the grain boundaries, the bulk O sites, can clearly be identified in Fig. 5 as the spherical, blue regions. It can also be seen that, on the PES of the $\Sigma 3$ grain boundary, the position, extension, and energy of the minima closest to the grain boundary are almost bulk-like. This indicates that the more close-packed character of the $\Sigma 3$ grain boundary is also reflected in the H solution energy profile. In contrast to this, the minimum of the H solution energy in the $\Sigma 11$ grain boundary appears significantly different from the bulk. The region at the interface with a low solution energy is much more extended, confirming that the more open structure of this grain boundary has a strong effect on the H solution energy. The absolute value of the solution energy is not dramatically reduced in the minimum in accordance with our previous observation.

To investigate whether volumetric effects can solely explain the H solution energies in the grain boundaries, we have determined the Voronoi volumes at each symmetry inequivalent adsorption site in the corresponding supercells. In Figs. 6(a) and 6(b), the solution energies are plotted versus the corresponding Voronoi volumes, indicating only a moderate correlation between the two quantities. The solid lines in the two plots show the corresponding solution energies in a tetrahedral/octahedral site in bcc/fcc bulk Fe for various volumes, respectively. These lines serve as a lower limit for most of the considered data. For those interstitial sites in the grain boundary structure that have a symmetric, tetrahedral/octahedral coordination, the Voronoi volume is
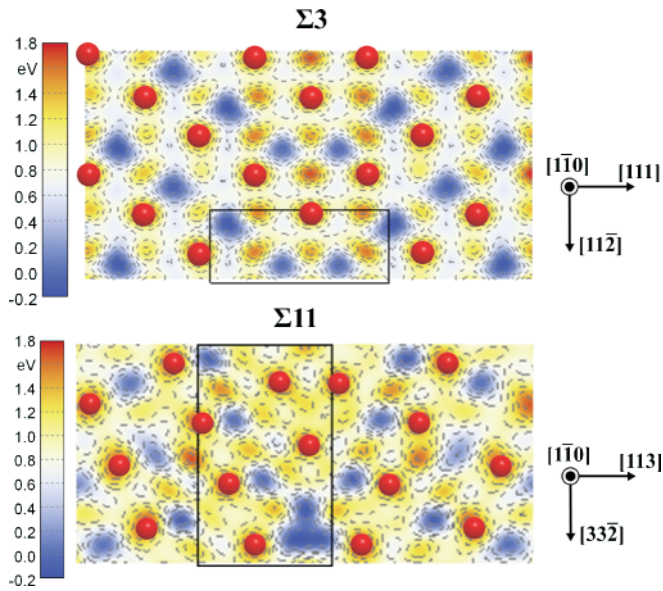
FIG. 5. (Color online) Cuts of the potential energy surfaces along $(1\bar{1}0)$ planes for H in the fcc $\Sigma 3$ and $\Sigma 11$ grain boundaries, respectively. Hydrogen solution energies are given in eV. The black boxes indicate the regions considered for the diffusion pathways in Figs. 9 and 12.

FIG. 6. (Color online) Solution energy, ΔE, of hydrogen as a function of the Voronoi volume of the interstitial site in tetrahedral sites in bcc (top graph) and octahedral sites in fcc Fe (bottom graph) and in various adsorption sites within the bcc $\Sigma 3$, bcc $\Sigma 5$, fcc $\Sigma 3$, and fcc $\Sigma 11$ Fe grain boundaries. The strain dependence of the H solution energies in the energetically favorable bulk sites of bcc and fcc Fe are given by solid black lines.

still a useful indicator. However, for distorted tetrahedral/octahedral and/or differently coordinated sites, the solution energy is typically higher than predicted by a pure volume argument, i.e., the benefit of a more open volume (excess volume) is largely compensated by an unfavorable atomic configuration.

More specifically, within the close-packed structures of the low-energy $\Sigma 3$ grain boundaries in both bcc/fcc Fe, most interstitial sites are only slightly distorted tetrahedral/octahedral sites that compare reasonably to the corresponding interstitial sites in the bulk material, which is also reflected in the two graphs in Fig. 6. At the interface, however, in the case of the $\Sigma 3$ bcc grain boundary, a slightly elongated octahedral interstitial site, cf. Fig. 7, is available. This site has a significantly lower solution energy (open, red circle in Fig. 6, top graph), which is comparable to the value in octahedrally coordinated sites considered for fcc (Fig. 6, bottom graph).

Within the more open $\Sigma 5$ bcc and $\Sigma 11$ fcc grain boundary structures, the distortion of interstitial sites close to the grain boundary is much larger and different types of coordination can be found; cf. Fig. 7. The solution energy in these distorted interstitial sites cannot simply be related to the Voronoi volumes mainly due to a rather asymmetric binding situation. In both grain boundaries, the distorted interstitial sites have much lower solution energies, so that both the $\Sigma 5$ and $\Sigma 11$ grain boundaries act as traps for H atoms of ~ 0.4 and ~ 0.1 eV, respectively. In both cases, the energy gain is slightly lower than the trapping energy in a vacancy of 0.6 and 0.3 eV for bcc Fe[10] and fcc Fe,[13] respectively. Within a vacancy hydrogen also binds asymmetrically, being much closer to one of the surrounding Fe atoms than to all others, and up to four H atoms can occupy a vacancy still yielding an energy gain. The relatively large interstitial voids at the interface appear to provide a comparable binding situation and it might also be
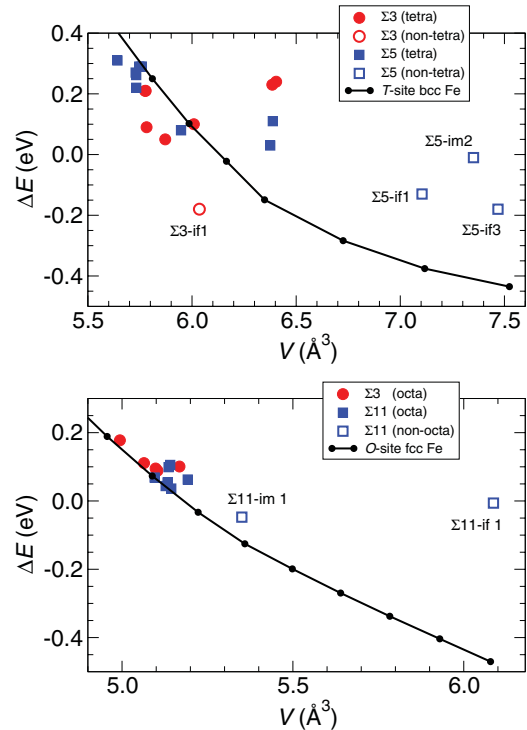
possible to accommodate more than one H atom in such an interstitial site.

V. EFFECT OF H ON CRACK FORMATION ALONG α- AND γ-IRON GRAIN BOUNDARIES

In the previous section, we have shown that both open grain boundary structures, the $\Sigma 5$ in α-Fe and the $\Sigma 11$ in γ-Fe, as well as the more close-packed $\Sigma 3$ grain boundary in α-Fe with a special interstitial site, provide traps for hydrogen. In this section, we use Griffith's theory[65] to estimate the effect of a potential hydrogen accumulation in the grain boundaries on crack formation along the grain boundary. According to Griffith's theory, the critical strain σ_c for crack formation is roughly proportional to the inverse square root of the flaw length a:

$$\sigma_c \sqrt{a} = C. \qquad (3)$$

The proportionality factor C is determined by the Young's modulus E of the material and the surface energy γ along the readily formed crack,

$$C = \sqrt{\frac{2E\gamma}{\pi}}. \qquad (4)$$

If fracture occurs along the grain boundary, we may calculate the corresponding surface energy as the difference between the energy of the newly created surface and the grain boundary.
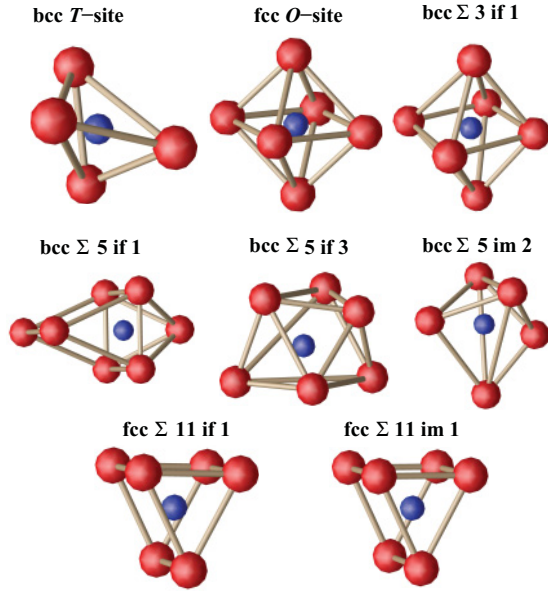
FIG. 7. (Color online) Local coordination of interstitial sites: most interstitial sites resemble slightly distorted tetrahedral/octahedral sites as in bcc/fcc iron, respectively. Only sites that exhibit a significantly different coordination (open symbols in Fig. 6) are shown; labels are according to Tables II and III.

For the clean grain boundary without hydrogen, the surface energy $\gamma_{\text{crack}}^{\text{clean}}$ is given as

$$\gamma_{\text{crack}}^{\text{clean}} = \frac{2E_{\text{surf}}^{\text{tot}} - E_{\text{GB}}^{\text{tot}} - \Delta N E_{\text{bulk}}^{\text{tot}}}{4A}$$
$$= \gamma_{\text{surf}}^{\text{clean}} - 1/2\gamma_{\text{GB}}^{\text{clean}}. \qquad (5)$$

Here $E_{\text{surf}}^{\text{tot}}$ is the total energy of the supercell containing the surface (one "half" of the grain boundary with N_{surf} Fe atoms), $E_{\text{GB}}^{\text{tot}}$ is the total energy of the supercell containing the grain boundary (with N_{GB} Fe atoms), and A is the area of the surface, respectively, interface. If the supercells of the grain boundary and surface structure are not commensurate, the excess Fe atoms have to be taken from or put into a bulk reservoir, i.e., $\Delta N = 2N_{\text{surf}} - N_{\text{GB}}$, and $E_{\text{bulk}}^{\text{tot}}$ is the energy of an Fe atom in the corresponding bulk structure. $\gamma_{\text{surf}}^{\text{clean}}$ is the surface energy of the corresponding free surface and $\gamma_{\text{GB}}^{\text{clean}}$ is the interface energy of the grain boundary. For the three grain boundary structures, we obtain $\gamma_{\text{crack}}^{\text{clean}}$ energies of 116 meV/Å^2, 187 meV/Å^2, and 154 meV/Å^2 for the $\Sigma 5$ bcc, $\Sigma 11$ fcc, and $\Sigma 3$ bcc Fe grain boundary, respectively.

If hydrogen accumulates in the grain boundary and is present during the crack formation, such that the resulting surfaces are covered with hydrogen, the corresponding surface energies are given by

$$\gamma_{\text{crack}}^{\text{hyd}} = \gamma_{\text{crack}}^{\text{clean}} + n^{\text{cov}} \Delta E_{\text{GB} \rightarrow \text{surf}}. \qquad (6)$$

Here $\Delta E_{\text{GB} \rightarrow \text{surf}} = \Delta E_b^{\text{H/surf}} - \Delta E_b^{\text{H/GB}}$ is the difference in binding energies of hydrogen to the grain boundary and to the surface, respectively, and n^{cov} is the number of H atoms per surface area. From Eq. (6), it can be seen that the energy to form a crack along the grain boundary will be lowered in the presence of hydrogen if $\Delta E_{\text{GB} \rightarrow \text{surf}}$ is negative, i.e., if

TABLE IV. Computed γ^{clean} (meV/Å^2), γ^{hyd} (meV/Å^2), n^{cov} (1/Å^2), and $\sigma_c^{\text{hyd}}/\sigma_c^{\text{strain}}$ for various grain boundaries in α- and γ-Fe.

	$\gamma_{\text{crack}}^{\text{clean}}$	$\gamma_{\text{crack}}^{\text{hyd}}$	n^{cov}	$\sigma_c^{\text{hyd}}/\sigma_c^{\text{clean}}$
$\Sigma 5$ bcc	116	103	0.08	0.94
$\Sigma 11$ fcc	187	133	0.10	0.84
$\Sigma 3$ bcc	154	103	0.10	0.82

hydrogen binds more strongly to the surface than to the grain boundary interface.

For the bcc $\Sigma 5$ grain boundary, we have determined $\Delta E_{\text{GB} \rightarrow \text{surf}} = -0.17$ eV; for the $\Sigma 11$ fcc and $\Sigma 3$ bcc, the difference in binding energy is much larger with -0.54 and -0.45 eV, respectively. For all three grain boundaries, the values are negative indicating that hydrogen facilitates the fracture along the grain boundary.

The effect also strongly depends on the hydrogen coverage. The actual hydrogen coverage at the surface, n^{cov}, depends on the experimental setup. Here we assume hydrogen-rich conditions for which all available sites in the grain boundary are occupied by H atoms, yielding a coverage of 0.08/Å^2, 0.1/Å^2, and 0.1/Å^2 for the $\Sigma 5$ bcc, $\Sigma 11$ fcc, and $\Sigma 3$ bcc Fe grain boundaries, respectively. Using these values and Eqs. (3) and (4), we can estimate the effect of hydrogen accumulation on the critical strain for crack formation under hydrogen-rich conditions for various grain boundary structures:

$$\sigma_c^{\text{hyd}}/\sigma_c^{\text{clean}} = \sqrt{\frac{\gamma^{\text{hyd}}}{\gamma^{\text{clean}}}}. \qquad (7)$$

The results are summarized in Table IV. We obtain $\sigma_c^{\text{hyd}}/\sigma_c^{\text{clean}}$ of 0.94, 0.84, and 0.82 for the $\Sigma 5$ bcc, $\Sigma 11$ fcc, and $\Sigma 3$ bcc Fe grain boundaries, respectively. This means that hydrogen accumulation in the various grain boundary structures can lower the critical strain for crack formation along the grain boundary by 6%, 16%, and 18%, respectively, such that we expect that for the three interfaces hydrogen acts as an embrittler. If we assume that H readily diffuses towards the free surface upon crack formation the nominal hydrogen coverage would double, yielding a full monolayer at the free surface. Within our simple approximation, the critical strain would then be reduced even further by 12%, 35%, and 36% for bcc $\Sigma 5$, fcc $\Sigma 11$, and bcc $\Sigma 3$, respectively.

As the Griffith's criterion may be seen only as a rough estimate, it is difficult to provide a quantitative statement regarding the lowering of the critical strain. Nevertheless, from Eqs. (6) and (7), it is clear that the effect increases with increasing coverage, n^{cov}, a larger, negative difference in the binding energy to the surface and interface, $\Delta E_{\text{GB} \rightarrow \text{surf}}$, and a smaller surface energy for the formation of a crack along the clean grain boundary, $\gamma_{\text{crack}}^{\text{clean}}$. The hydrogen coverage at the grain boundary will be large if there is a high mobility of hydrogen and the hydrogen atoms are trapped at the interface. Assuming that there is hydrogen accumulated at the grain boundary, the decisive quantity is the difference in binding energy, $\Delta E_{\text{GB} \rightarrow \text{surf}}$. A strong binding to the grain boundary can then be favorable, whereas a strong binding to the corresponding surface enhances the decohesion, i.e.,

for grain boundaries with GB planes that provide very stable surface adsorption sites, the reduction of the critical strain due to hydrogen accumulation will be largest. This also applies to our findings for the three investigated grain boundaries. The effect is smallest for the $\Sigma5$ bcc grain boundary, where the energy gain for a hydrogen atom at the surface compared to the grain boundary interface is smallest. This might be explained by the fact that the $\Sigma5$ grain boundary offers an extremely stable adsorption site at the interface and the corresponding (310) surface is a rather high index surface. On the other hand, the (113) grain boundary plane of the $\Sigma11$ fcc structure is also a rather high index surface, but here the binding to the interface is less pronounced and thus the difference in binding energies is large. In the $\Sigma3$ bcc grain boundary, we encounter yet another situation: the binding energy to the interface is as strong as in the $\Sigma5$ grain boundary, but the corresponding (112) surface offers likewise a very stable adsorption site, leading again to larger energy gain for H atoms at the surface as compared to the interface and thus an increased embrittlement effect.

VI. MOBILITY OF H WITHIN α- AND γ-IRON GRAIN BOUNDARIES

To explain the significant role of grain boundaries in H embrittlement, it is important to understand how hydrogen diffusion is affected by the presence of grain boundaries. This rather complex problem is difficult to address both experimentally and theoretically, and it is still debated if grain boundaries provide fast diffusion channels that enhance the diffusivity of hydrogen or not.[66–71]

A prerequisite for diffusion within grain boundaries is the attraction of hydrogen to the grain boundaries. As discussed in Sec. IV, the more open grain boundary structures $\Sigma5$ and $\Sigma11$ provide traps for H atoms. For the more close-packed $\Sigma3$ grain boundary structure in bcc Fe, a special interstitial site is available at the interface that attracts hydrogen, whereas in the case of fcc Fe hydrogen is slightly repelled from the $\Sigma3$ grain boundary. This information alone, however, is not sufficient for understanding H mobilities. We further need to consider the diffusion paths connecting these special sites and in particular the barriers for diffusion within and towards the interface.

We have used two different strategies to obtain this information. On the one hand, the concept of the PES, for which examples were already shown in Fig. 5, can be used to evaluate diffusion paths. In this case, the hydrogen solution energies mainly at the high-symmetry transition points and the local minima next to them were calculated directly, and plane wave interpolations have been applied in between. On the other hand, we determined the diffusion paths between different sites employing the nudged-elastic band (NEB) method.[72–74] Here, the migration pathway is represented by several images between two fully relaxed end points and each image is relaxed until the perpendicular forces with respect to the minimum energy path are less than a given tolerance, which was set to 0.05 eV/Å in our case. This method is, in particular, advantageous if the exact position of the transition point is unknown or if detailed information about the energy profile along the transition path is important.
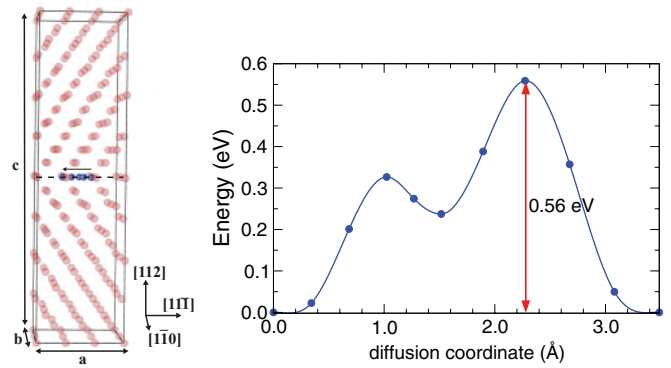

FIG. 8. (Color online) Hydrogen diffusion path within the $\Sigma3$ grain boundary in bcc Fe. H migrates along the a axis with an overall diffusion barrier of $\sim$0.6 eV. The left plot illustrates the position of the H atom at various points along the diffusion path.

A. H diffusion within $\Sigma3$ grain boundaries

The diffusion of H atoms within the $\Sigma3$ grain boundary in bcc Fe was investigated employing the above-mentioned NEB calculations.[75] For the diffusion within the grain boundary plane, we obtain a migration barrier of $\sim$0.6 eV as shown in Fig. 8. Hydrogen at the interface diffuses to its equivalent site along the a axis within the grain boundary plane. Since H interstitials can cause relatively large distortions in the close-packed $\Sigma3$ grain boundary structure, it was difficult within our limited supercell size to perform similar NEB studies for the escape barrier for H diffusion from the interface to the bulk region. However, the escape barrier is expected to be dominated by the difference in solution energies between the interface and the interstitial site in the bulk region. Since these values are -0.18 and 0.25 eV, respectively, we estimate the escape barrier to be larger than 0.5 eV.

For the $\Sigma3$ grain boundary in fcc Fe, we investigated our results from the 3D PES, of which a cut along a $(1\bar{1}0)$ plane is shown in Fig. 9. As discussed in Sec. IV, this $\Sigma3$ grain boundary repels H, i.e., the potential energy at the local minimum in the grain boundary is higher than at the octahedral interstitial sites in bulk fcc Fe. In addition, the saddle points for H diffusion in the vicinity of the grain boundary (0.9 eV) are also higher in energy than the saddle points for bulk diffusion (0.6 eV). Based on these findings, we conclude that the $\Sigma3$ will act as an obstacle (2D barrier wall) for the H diffusion in fcc Fe, constraining the diffusion mainly to the bulk region.

B. H diffusion within the open $\Sigma5$ and $\Sigma11$ grain boundaries

The migration of H atoms towards and within the $\Sigma5$ grain boundary in bcc-Fe was studied employing NEB calculations.[76] For the diffusion within the grain boundary plane, two adjacent, equivalent interface sites (if3 sites; cf. Table III) along the b axis ([001] direction) were chosen as the initial and final point of the diffusion pathway. The energy along the relaxed diffusion pathway is shown in Fig. 10 yielding a diffusion barrier of $\sim$0.3 eV for H atoms parallel to the grain boundary interface. In the left plot of Fig. 10, the migration pathway is illustrated by showing the position of hydrogen at various points along the path. It can be seen that hydrogen remains very close to the interface while diffusing
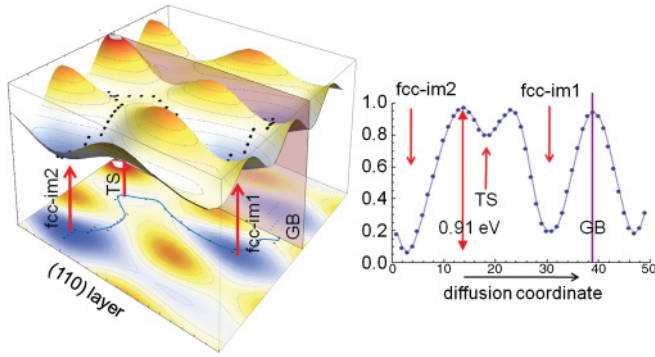
FIG. 9. (Color online) Diffusion for a H interstitial close to the $\Sigma 3$ grain boundary in fcc iron. The pathway lies within the part of the $(1\bar{1}0)$ plane indicated in Fig. 5. The overall barrier for H to escape from the interface region is computed to be 0.9 eV.

from one interface site to the next. Next we investigated the diffusion of H atoms perpendicular to the grain boundary interface along the c axis ([310] direction). Interface site 3 was again set as the initial state and a T site within the bulk region was chosen as the final state. The energy along the relaxed migration pathway is shown in Fig. 11 together with an illustration of the H position at various points along the diffusion path. The overall energy barrier to diffuse away from the grain boundary interface is $\sim$0.60 eV, passing through an intermediate, metastable state, with a barrier of $\sim$0.40 eV. The high barrier is mainly due to the large energy difference between the initial and final state configurations, as the hydrogen is strongly trapped in the grain boundary plane. The energy barrier for the diffusion from the bulk region towards the interface region, on the other hand, is very small with $\sim$0.1 eV and comparable to the bulk diffusion barrier.

Within the $\Sigma 11$ fcc Fe grain boundary, the potential energy in the grain boundary interface is also lower than in the octahedral interstitial sites (Fig. 12). Furthermore, the investigation of the migration barriers next to the local minima in the grain boundary revealed that the $\Sigma 11$ grain boundary also acts as a trap for H. The migration barrier to escape from this local minimum in the grain boundary to the bulk region is $\sim$1.1 eV, approximately 0.4 eV higher than the migration barrier in the bulk region (0.6 eV). However, as can be seen in Fig. 13, close to the $\Sigma 11$ grain boundary there exists a diffusion
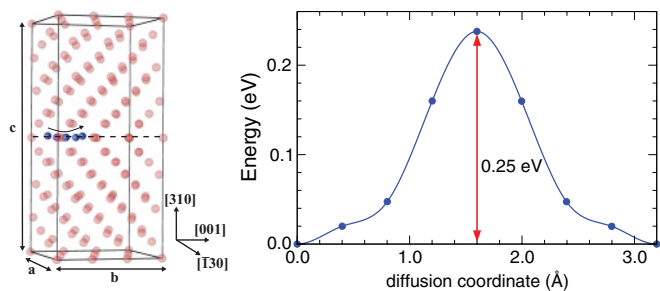

FIG. 10. (Color online) Diffusion pathway for a H interstitial within the interface region of the $\Sigma 5$ grain boundary in bcc Fe. The overall barrier for hydrogen to diffuse within the interface region is computed to be 0.25 eV. The diffusion path starts in interface site if3 and ends in the equivalent if3 site one lattice vector along the b axis.
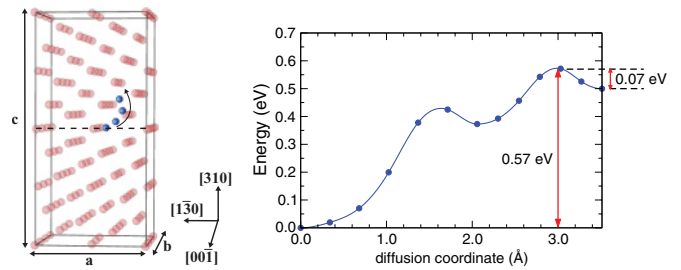

FIG. 11. (Color online) Diffusion pathway for a H interstitial to move from the interface plane towards the bulk region in the $\Sigma 5$ grain boundary in bcc iron. The overall barrier for a H interstitial to escape from the interface region is computed to be 0.6 eV.

path in the $[1\bar{1}0]$ direction [perpendicular to the $(1\bar{1}0)$ plane] with a migration barrier of 0.7 eV, which is very similar to the bulk value. Once hydrogen is outside the trapping site in the boundary, it can diffuse along the grain boundary plane with a barrier of approximately 0.1 eV, indicating a very efficient diffusion channel.

C. Comparison of H diffusion within α- and γ-Fe grain boundaries

The presence of grain boundaries in the bulk material has a significant influence on the diffusion of hydrogen in both α- and γ-Fe. The more open grain boundary structures, the $\Sigma 5$ bcc and $\Sigma 11$ fcc, both provide special interstitial sites for H at the interface that are energetically favorable. The diffusion barriers between these rather stable interstitial sites and the bulk material are higher (0.6 eV for $\Sigma 5$ in bcc Fe and 1.1 eV for $\Sigma 11$ in fcc Fe) than within the bulk material ($\sim$0.1 eV[54] between tetrahedral sites in bcc Fe and 0.6 eV[39] between octahedral sites in fcc Fe). This indicates that within the bulk material hydrogen can readily diffuse towards the grain boundary (faster in bcc than in fcc Fe), but once it has reached the interface it has to overcome larger barriers to escape again, i.e., it will effectively be trapped near the interface. However, for both open grain boundaries, diffusion paths for hydrogen with barriers ($\sim$0.25 eV for $\Sigma 5$ in bcc Fe and 0.7 eV for $\Sigma 11$ in fcc Fe) comparable to the bulk values exist. This means that H atoms within the grain boundaries are still mobile, especially compared to diffusion away from the grain boundary interfaces, but they diffuse slower than in the
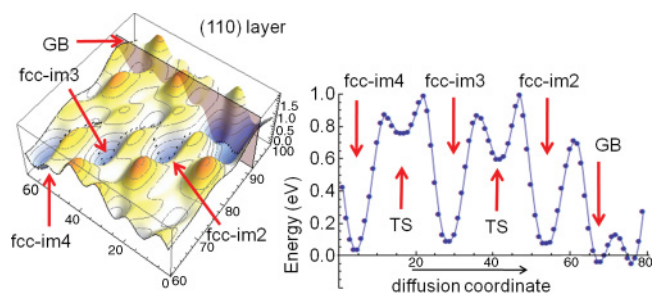

FIG. 12. (Color online) Diffusion for a H interstitial perpendicular to the $\Sigma 11$ grain boundary in fcc iron. The pathway lies within the part of the $(1\bar{1}0)$ plane indicated in Fig. 5. The overall barrier for H to escape from the interface region is computed to be 1.1 eV.
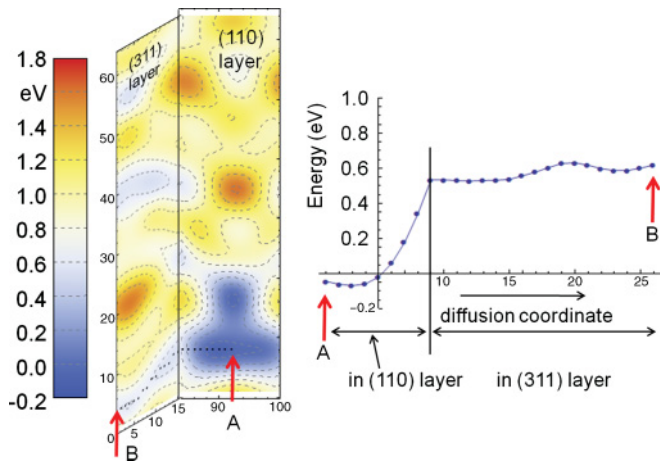
FIG. 13. (Color online) Diffusion pathway for a H interstitial close to the $\Sigma 11$ grain boundary in fcc iron. After a displacement within the $(1\bar{1}0)$ plane out of the center of the grain boundary (point A), the displayed motion occurs in the $[1\bar{1}0]$ direction [within the (113) plane parallel and perpendicular to the $(1\bar{1}0)$ plane]. The overall barrier for this pathway is 0.7 eV.

bulk region. The grain boundaries thus influence the preferred direction of diffusion, but do not increase the diffusivity. If the grain boundary interface is saturated with H atoms, it is not obvious from pure energetic arguments how hydrogen diffusion is affected and we are currently investigating the concentration dependent diffusion behavior employing kinetic Monte Carlo simulations.

The close-packed $\Sigma 3$ grain boundaries are even more a barrier for the diffusion of hydrogen. For the $\Sigma 3$ bcc grain boundary, the H migration barrier within the interface is as high as 0.6 eV. Thus, if H interstitials are trapped at the $\Sigma 3$ grain boundary, they become immobile. As discussed, the $\Sigma 3$ grain boundary in fcc Fe is repulsive to hydrogen, i.e., it is unfavorable for H atoms to diffuse towards the grain boundary interface.

In summary, we find that none of the investigated grain boundaries provides a fast diffusion channel for H atoms in the dilute limit. Within the more open grain boundary structures, a preferred diffusion direction along the interface is found at low hydrogen coverage, which is much slower than bulk diffusion. The close-packed grain boundaries, on the other hand, are predicted to act as two-dimensional barriers for hydrogen diffusion.

VII. CONCLUSIONS

We have investigated the interaction of H interstitials with open and close-packed grain boundary structures within the two most relevant phases of iron in steels: the ferritic α- and austenitic γ-Fe. The phases have been considered in the ferromagnetically saturated and the nonmagnetic configuration, respectively. The latter is an approximation for a more realistic paramagnetic description of the austenite phase, which is currently not feasible, leaving additional corrections due to the delicate interplay of hydrogen with the special magnetic configuration at the grain boundary for future research. We focused on three aspects: the stability of hydrogen

in the vicinity of the grain boundaries, the effect of hydrogen on the fracture strength of the interface, and the mobility of hydrogen towards and within the grain boundary planes.

The solution energy of hydrogen within the different grain boundary structures strongly depends on the local coordination of the corresponding interstitial site and is only moderately correlated with the actual volume of the interstitial site. Within the close-packed, low-energy $\Sigma 3$ grain boundaries, the available interstitial sites are very similar to the tetrahedral and octahedral sites in the corresponding bulk structures. Only directly at the interface different interstitial sites are available, leading to an attraction of hydrogen within the bcc $\Sigma 3$ structure and a repulsion from the fcc $\Sigma 3$ grain boundary. Within the open grain boundary structures, $\Sigma 5$ bcc and $\Sigma 11$ fcc, various different interstitial sites are available, generally providing favorable binding sites for H atoms, which implies that hydrogen is trapped at the grain boundary.

For those structures where H accumulation at the grain boundary is energetically favored, the critical strain required to fracture the material is reduced by the presence of hydrogen, i.e., hydrogen acts as an embrittler. Within our estimate, the effect is dominated by the difference in binding energy of H to the interface and to the corresponding free surface. Thus the effect appears to be smallest for the open $\Sigma 5$ bcc structure, which provides large cavities at the interface where the hydrogen is almost as strongly bound as to the surface. A much larger influence of hydrogen accumulation on the critical strain is found for the $\Sigma 11$ fcc and $\Sigma 3$ bcc grain boundaries, where the binding energy of hydrogen is considerable larger at the surface as compared to the interface.

The grain boundaries also have a significant influence on the diffusion behavior of hydrogen. None of the investigated grain boundaries provides a fast diffusion channel for H atoms, but the more open structures, $\Sigma 5$ bcc and $\Sigma 11$ fcc, favor diffusion along the grain boundary plane and might thus direct hydrogen diffusion towards other defects, such as grain boundary junctions or dislocations. The close-packed grain boundary structures do not promote hydrogen diffusion and might even represent two-dimensional barriers to hydrogen diffusion.

Both hydrogen accommodation and diffusion depend sensitively on the local geometric structure and it is thus not straightforward to deduce simple rules that describe the observed behavior and are generally applicable. Still, there is a tendency for the more open interface structures in both α- and γ-Fe to accommodate hydrogen more easily and to provide diffusion pathways that can determine the preferred direction of hydrogen diffusion within these structures.

*jutta.rogal@rub.de

[1] R. Wu, A. J. Freeman, and G. B. Olson, Phys. Rev. B **53**, 7504 (1996).

[2] W. T. Geng, A. J. Freeman, R. Wu, and G. B. Olson, Phys. Rev. B **62**, 6208 (2000).

[3] W. T. Geng, A. J. Freeman, and G. B. Olson, Phys. Rev. B **63**, 165415 (2001).

[4] R. Wu, A. J. Freeman, and G. B. Olson, Science **15**, 376 (1994).

[5] M. Yamaguchi, Y. Nishiyama, and H. Kaburaki, Phys. Rev. B **76**, 035418 (2007).

[6] R. Yang, R. Huang, Y. Wang, H. Ye, and C. Wang, J. Phys. Condens. Matter **15**, 8339 (2003).

[7] W. T. Geng, A. J. Freeman, R. Wu, C. B. Geller, and J. E. Raynolds, Phys. Rev. B **60**, 7149 (1999).

[8] J. P. Hirth, Metall. Mater. Trans. A **11**, 861 (1980).

[9] P. Novak, R. Yuan, B. Somerday, P. Sofronis, and R. Ritchie, J. Mech. Phys. Solids **58**, 206 (2010).

[10] A. Ramasubramaniam, M. Itakura, M. Ortiz, and E. Carte, J. Mater. Res. **23**, 2757 (2008).

[11] M. Wen, S. Fukuyama, and K. Yokogawa, Acta Mater. **51**, 1767 (2003).

[12] L. Zhong, R. Wu, A. J. Freeman, and G. B. Olson, Phys. Rev. B **62**, 13938 (2000).

[13] R. Nazarov, T. Hickel, and J. Neugebauer, Phys. Rev. B **82**, 224104 (2010).

[14] C. D. Beachem, Metall. Trans. **3**, 437 (1972).

[15] H. K. Birnbaum, Mater. Sci. Eng. A **176**, 191 (1994).

[16] J. von Pezold, L. Lymperakis, and J. Neugebauer, Acta Mater. **59**, 2969 (2011).

[17] D. Psiachos, T. Hammerschmidt, and R. Drautz, Acta Mater. **59**, 4255 (2011).

[18] R. A. Oriani and P. H. Josephic, Acta Metall. **22**, 1065 (1974).

[19] R. A. Oriani and P. H. Josephic, Acta Metall. **25**, 979 (1977).

[20] R. A. Oriani, Annu. Rev. Mater. Sci. **8**, 327 (1978).

[21] S. Lee and D. Unger, Eng. Fract. Mech. **31**, 647 (1988).

[22] W. W. Gerberich, T. Livne, X. F. Chen, and M. Kaczorowski, Metall. Mater. Trans. A **19**, 1319 (1988).

[23] S. B. Gesari, M. E. Pronsato, and A. Juan, Appl. Surf. Sci. **187**, 207 (2002).

[24] A. Anderson, J. Chem. Phys. **62**, 1187 (1975).

[25] P. Hohenberg and W. Kohn, Phys. Rev. **136**, B864 (1964).

[26] W. Kohn and L. J. Sham, Phys. Rev. **140**, A1133 (1965).

[27] J. Rice and J. Wang, Mater. Sci. Eng. A **107**, 23 (1989).

[28] P. M. Anderson, J. S. Wang, and J. R. Rice, in *Innovations in Ultrahigh-Strength Steel Technology*, edited by G. B. Olson, M. Azrin, and E. S. Wright, Proceedings of the 34th Sagamore Army Materials Research Conference (Government Printing Office, Washington, DC, 1990), p. 619.

[29] O. Grässel, L. Krüger, G. Frommeyer, and L. Meyer, Int. J. Plast. **16**, 1391 (2000).

[30] G. Frommeyer, U. Brüx, and P. Neumann, ISIJ Int. **43**, 438 (2003).

[31] S. Allain, J. Chateau, and O. Bouaziz, Mater. Sci. Eng. A **387**, 143 (2004).

[32] W. Godoi, N. Kuromoto, A. Guimaraes, and C. Lepienski, Mater. Sci. Eng. A **354**, 251 (2003).

[33] S. Fukuyama, D. Sun, L. Zhang, and K. Yokogawa, Journal of the Japan Institute of Metals **67**, 456 (2003).

[34] L. Tsay, S. Yu, and R.-T. Huang, Corros. Sci. **49**, 2973 (2007).

[35] Y. Tsunoda, J. Phys. Condens. Matter **1**, 10427 (1989).

[36] O. Mryasov, A. Liechtenstein, L. M. Sandratskii, and V. Gubanov, J. Phys. Condens. Matter **3**, 7683 (1991).

[37] M. Körling and J. Ergon, Phys. Rev. B **54**, R8293 (1996).

[38] D. W. Boukhvalov, Y. N. Gomostyrev, M. I. Katsnelson, and A. I. Lichtenstein, Phys. Rev. Lett. **99**, 247205 (2007).

[39] L. Ismer, T. Hickel, and J. Neugebauer, Phys. Rev. B **81**, 094111 (2010).

[40] N. Gao, C.-C. Fu, M. Samaras, R. Schäublin, M. Victoria, and W. Hoffelner, J. Nucl. Mater. **385**, 262 (2009).

[41] L. Lymperakis, M. Friak, and J. Neugebauer, Eur. Phys. J. **177**, 41 (2009).

[42] P. E. Blöchl, Phys. Rev. B **50**, 17953 (1994).

[43] G. Kresse and D. Joubert, Phys. Rev. B **59**, 1758 (1999).

[44] G. Kresse and J. Hafner, Phys. Rev. B **47**, 558(R) (1993).

[45] G. Kresse and J. Furthmüller, Phys. Rev. B **54**, 11169 (1996).

[46] J. P. Perdew, J. A. Chevary, S. H. Vosko, K. A. Jackson, M. R. Pederson, D. J. Singh, and C. Fiolhais, Phys. Rev. B **46**, 6671 (1992).

[47] J. P. Perdew, J. Chevary, S. Vosko, K. A. Jackson, M. R. Pederson, D. J. Singh, and C. Fiolhais, Phys. Rev. B **48**, 4978 (1993).

[48] H. J. Monkhorst and J. D. Pack, Phys. Rev. B **13**, 5188 (1976).

[49] J. Staunton, B. L. Gyorffy, A. J. Pindor, G. M. Stocks, and H. Winter, J. Magn. Magn. Mater. **45**, 15 (1984).

[50] B. Alling, T. Marten, and I. A. Abrikosov, Phys. Rev. B **82**, 184430 (2010).

[51] R. Kohlhaas, P. Dunner, and N. Schmitz-Prange, Z. Angew. Phys. **23**, 245 (1967).

[52] E. G. Moroni, G. Kresse, J. Hafner, and J. Furthmüller, Phys. Rev. B **56**, 15629 (1997).

[53] M. Čák, M. Šob, and J. Hafner, Phys. Rev. B **78**, 054418 (2008).

[54] D. E. Jiang and E. A. Carter, Phys. Rev. B **70**, 064102 (2004).

[55] Y. Tateyama and T. Ohno, Phys. Rev. B **67**, 174105 (2003).

[56] H. Krimmel, L. Schimmele, C. Elsässer, and M. Fähnle, J. Phys. Condens. Matter **6**, 7705 (1994).

[57] T. Hickel, A. Dick, B. Grabowski, F. Koermann, and J. Neugebauer, Steel Res. Int. **80**, 4 (2009).

[58] O. Grassel, L. Kruger, G. Frommeyer, and L. Meyer, Int. J. Plast. **16**, 1391 (2000).

[59] A. Abbasi, A. Dick, T. Hickel, and J. Neugebauer, Acta Mater. **59**, 3041 (2011).

[60] This is due to the asymmetric binding situation of the Fe atoms; the Fe atoms in the second layer exhibit a very short distance of 2.25 Å to their mirror atoms across the grain boundary and a distance of only 2.40 Å to the atoms in the third layer. These short nearest-neighbor distances lead to a decrease in the magnetic moment by 0.2 μ_B, as compared to the bulk value of 2.2 μ_B.

[61] Having lattice constants of $a = 8.87$ Å, $b = 8.39$ Å, and $c = 27.65$ Å.

[62] For larger distances z, a supercell with $a = 8.90$ Å, $b = 2.81$ Å, and $c = 36.57$ Å is used.

[63] L. Ismer, T. Hickel, and J. Neugebauer (unpublished).

[64] S. Boeck, S. Freysoldt, A. Dick, L. Ismer, and J. Neugebauer, Comput. Phys. Commun. **182**, 543 (2011).

[65] A. Griffith, Philos. Trans. R. Soc. London A **221**, 163 (1921).

[66] K. Ichitani and M. Kanno, Sci. Technol. Adv. Mater. **4**, 545 (2003).

[67] A. Pedersen and H. Jónsson, Acta Mater. **57**, 4036 (2009).

[68] M. Ichimura, Y. Sasajima, and M. Imabayashi, Mater. Trans. JIM **32**, 1109 (1991).

[69]B. Szpunar, L. J. Lewis, I. Swainson, and U. Erb, Phys. Rev. B **60**, 10107 (1999).

[70]T. Harris and R. Latanision, Metall. Trans. A **22**, 351 (1991).

[71]M. Aucouturier, J. Phys. Colloq. **43**, 175 (1982).

[72]H. Jónsson, G. Mills, and K. W. Jacobsen, in *Classical and Quantum Dynamics in Condensed Phase Simulations*, edited by B. J. Berne, G. Ciccotti, and D. F. Coker (World Scientific, Singapore, 1998), pp. 385–404.

[73]G. Henkelman, B. P. Uberuaga, and H. Jónsson, J. Chem. Phys. **113**, 9901 (2000).

[74]G. Henkelman and H. Jónsson, J. Chem. Phys. **113**, 9978 (2000).

[75]For the NEB calculations, a 144 atom supercell with lattice constants of $a = 7.99$ Å, $b = 7.33$ Å, and $c = 27.97$ Å was used; the error in the energy barrier due to the interface-interface interaction is estimated to be less than 40 meV.

[76]For the NEB calculations, a 120 atom supercell with lattice constants of $a = 8.84$ Å, $b = 8.34$ Å, and $c = 18.71$ Å was used; the error in the energy barrier due the interface-interface interaction is estimated to be less than 40 meV.